Mass and density determination of porous nanoparticle films using a quartz crystal microbalance

van Ginkel, Hendrik Joost; Vollebregt, Sten; Schmidt-Ott, Andreas; Zhang, Guo Qi

DOI
10.1088/1361-6528/ac7811

Publication date
2022

Document Version
Final published version

Published in
Nanotechnology

PAPER • **OPEN ACCESS**

Mass and density determination of porous nanoparticle films using a quartz crystal microbalance

To cite this article: Hendrik Joost van Ginkel *et al* 2022 *Nanotechnology* **33** 485704

OPEN ACCESS
IOP Publishing
Nanotechnology

Nanotechnology **33** (2022) 485704 (8pp)
https://doi.org/10.1088/1361-6528/ac7811

Mass and density determination of porous nanoparticle films using a quartz crystal microbalance

Hendrik Joost van Ginkel[1], **Sten Vollebregt**[1,*], **Andreas Schmidt-Ott**[2] **and Guo Qi Zhang**[1,*]

[1] Electronic Components, Technology and Materials Group, Delft University of Technology, Delft, The Netherlands
[2] Materials for Energy Conversion and Storage, Delft University of Technology, Delft, The Netherlands

E-mail: h.j.vanginkel@tudelft.nl, s.vollebregt@tudelft.nl, g.q.zhang@tudelft.nl and a.schmidt-ott@tudelft.nl

Received 23 March 2022, revised 6 June 2022
Accepted for publication 13 June 2022
Published 9 September 2022

Abstract

A method is presented to directly measure the mass output of an impaction printer coupled with a spark ablation generator. It is based on a quartz crystal microbalance and shown to be reliable in quantifying mass deposition rate. Here, the method is demonstrated with an Au nanoparticle aerosol synthesized under several spark ablation and deposition settings. Changes in the deposition rate in response to changed synthesis conditions follow the spark ablation models on generation rate made in previous studies, validating this novel measurement method. In combination with the volume of a deposit, a good estimate of the film porosity can be made. The Au nanoparticle films synthesized here have a low porosity of 0.18 due to extensive restructuring and compaction on impact with the substrate. The porosity is found to be insensitive to deposition settings and is constant throughout the film. The simplicity and low cost of a quartz crystal microbalance setup make this an accessible method to determine porosity in porous thin films.

Supplementary material for this article is available online

Keywords: porous films, spark ablation, nanoparticles, quartz crystal microbalance, porosity, gold

(Some figures may appear in colour only in the online journal)

1. Introduction

Thin film technology is essential in the fabrication of advanced materials, nanotechnology, and microelectronics. In recent decades, the advancement in nanoparticle and nanoporous films have shown that such films can be superior to dense thin films due to their high surface-to-volume ratio, increased reactivity, lower melting point, and the porosity itself. For catalytic films, the increased reactivity and extreme surface to volume ratios reduce the amount of catalyst required or improve reaction efficiency [1–3]. These same properties make nanoparticles excellent sensing materials for chemical sensors [4–6]. In microelectronics, the low melting point of metallic nanoparticles has been used to create interconnects or as lead free solder alternative [7–9]. There are currently many synthesis methods available to make nanoparticles, each with their own advantages and disadvantages [5, 10–13]. Aerosol methods, in particular spark ablation, allow extreme variability in particle size and composition

* Authors to whom any correspondence should be addressed.

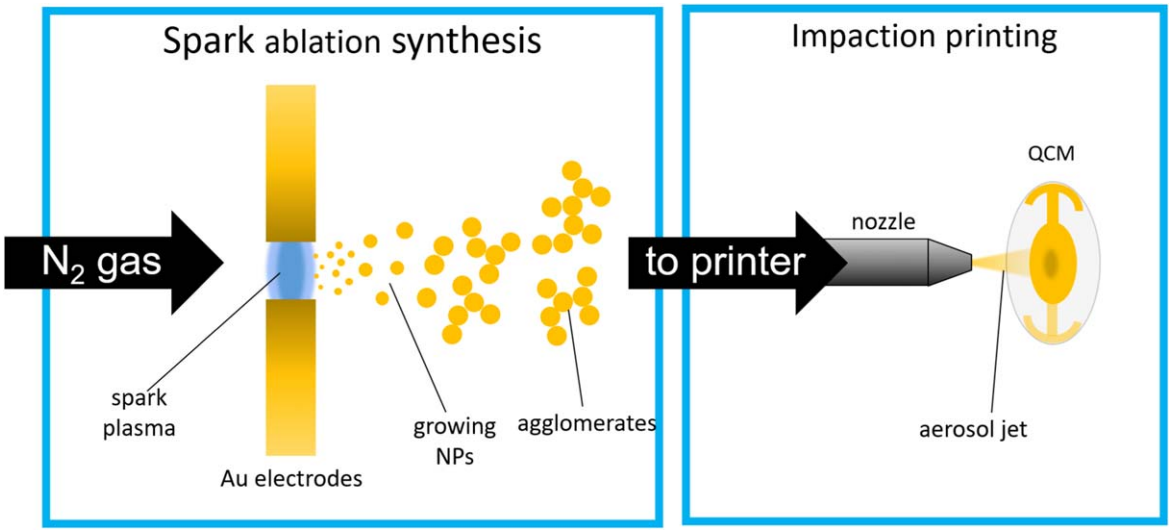

Figure 1. Schematic drawing of the spark ablation process and impaction on a QCM.

[13, 14]. In combination with direct deposition from the aerosol phase by impaction allows 3D printing of nanoparticle films onto most substrates. This production method has been successfully applied in catalysis [15, 16], gas sensors [17, 18], and surface enhanced Raman spectroscopy (SERS) [19, 20].

Despite the still growing number of application areas, characterization techniques for such nanoporous film are still lacking. Determining deposition rates or porosity, in particular, are still a challenge [21]. Material losses during synthesis and deposition are not precisely known and hard to estimate. Typical deposited mass is in the microgram range, for which almost no accurate measurement methods are available. Conventional mass balances are either inaccurate, difficult to use, expensive, or not available. Porosity measurement methods like the gas adsorption based Brunauer–Emmett–Teller method require larger quantities or are inaccurate with nanoporous materials [21, 22]. Quartz crystal microbalances (QCMs) are one of the few available options to measure such small masses reliably and without extensive calibration. Indeed, QCMs have been applied to study the size distribution of atmospheric aerosols [23–25]. For decades, QCMs have been used in process control for thin film deposition equipment such as sputtering [26] or atomic layer deposition [27]. QCMs are particularly useful for process control because they require no calibration, can achieve nanoscale resolution, and are cheap. Operation requires only a simple electric circuit and well-defined quartz crystals that are commonly available these days. The working principle of a QCM was first demonstrated by Sauerbrey in 1959 [28]. He found that oscillating quartz crystals have a very specific resonance frequency that is inversely related to its mass. The change in frequency by a change in mass is captured in the Sauerbrey equation [28]:

$$\Delta f = -C * \Delta mA, \tag{1}$$

where C is a material dependent constant and A the area of the QCM electrodes. Since Sauerbrey's paper, QCM theory has been improved to allow more application domains and more accurate devices [29–34]. They have since then been successfully used for thin film deposition process monitoring [26, 27], for gas sensors [35–37], as biochemical sensors [38, 39], and atmospheric sampling [23–25].

Similarly to the process control in thin film deposition tools, QCMs can be used to monitor the synthesis of porous, nanoparticle-based films. Here, we take it one step further by coupling mass measurements with volume or cross-section measurements to get the film density. In this work, we show that this methodology can be used to determine mass deposition rates and porosity during impaction printing of a metal nanoparticle aerosol generated by spark ablation. First, the validity of applying QCM microbalances to such nanoporous thin films is demonstrated. The effect of the gas jet and the deposition process on the QCM response is quantified. Next, the volume data is added and the porosity of the deposits is calculated and compared to literature.

2. Experimental

2.1. Nanoparticle generation and deposition

The synthesis of the nanoporous layers is done by spark ablation generation of a nanoparticle aerosol and inertial impaction as the deposition method, as drawn in figure 1. With spark ablation, repetitive microsecond sparks vaporize metallic electrodes, and extreme quenching by a carrier gas flow turns the vapor into nanoparticles. When reaching their final size, typically between 5 and 15 nm, they start to agglomerate instead of merging [13, 14, 40]. The carrier gas carries these agglomerates to the impaction printer where they are deposited. Impaction uses a pressure drop over a nozzle from 1bar to <1 mbar to accelerate the aerosol to supersonic speeds towards a sample. The inertia of the agglomerates causes them to impact on the substrate and become immobilized [41, 42]. By adjusting the printing speed and nozzle distance, one can adjust the width of the conical gas jet and, as a result, the width of the deposit. By moving the nozzle in

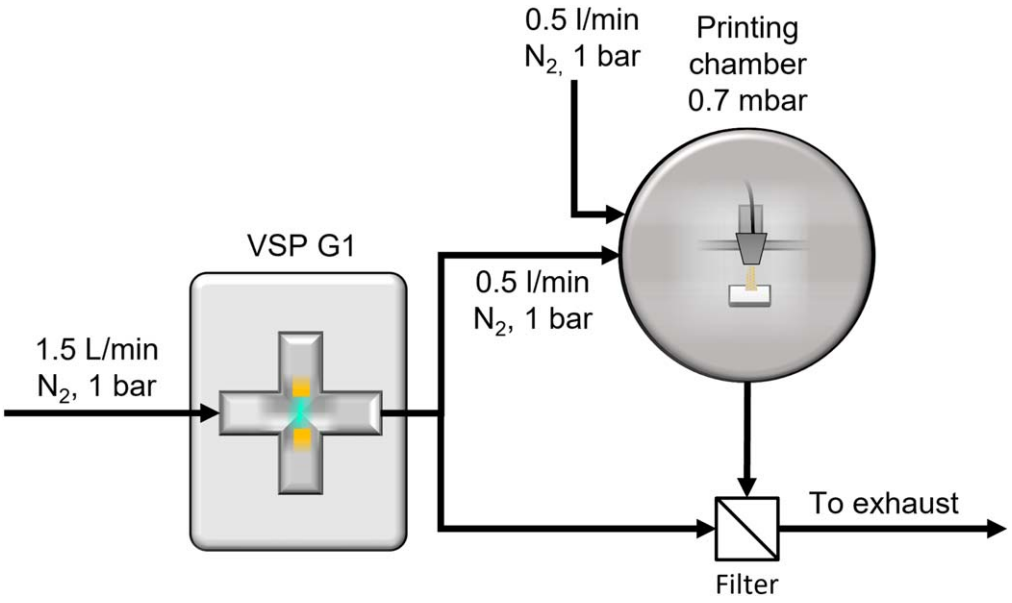

Figure 2. Diagram of the experimental setup showing gas inlets and pressures. Not all carrier gas is fed to the printer, the rest goes directly to the filter and exhaust.

the *XY*-plane, one can directly write complex patterns without lithography or masks. The spark ablation generator is a VSP G1 (VSParticle B.V.) and generates an Au nanoparticle aerosol from 99.999% Au electrodes (3 mm diameter). Operating conditions were set at 1.5 l min.$^{-1}$ N_2 at 1 bar was the carrier gas and the spark ablation discharge voltage was 1 kV. The average current was set to 2, 5, or 8 mA. The generator was connected to an impaction printer (VSParticle B.V., prototype) for nanoparticle deposition and was operated at a vacuum of 0.7 mbar. The nozzle has a diameter of 0.1 mm and a throughput of 0.32 l min^{-1}. The nozzle-substrate distance varied from 0.5 to 1.5 mm. To switch off the printing, clean N_2 gas flows through the nozzle so the setup has no dead volume at any time during operation. All gas connections and pressures are schematically drawn in figure 2.

2.2. Mass determination by QCM

The Sauerbrey equation, equation (1), can be used to translate the change of resonance frequency to mass but is only valid if the deposition is uniform over the entire electrode area, the film resonates with the crystal, and the deposited mass is less than 2% of the crystal's mass [28, 31]. The latter condition was clearly satisfied, as the film thickness was kept below 1 um. The first condition can be satisfied by printing on the entire electrode using concentric circles starting in the middle (see supporting information figure S1 available online at stacks.iop.org/NANO/33/485704/mmedia). By spacing them 0.2 mm apart, they will overlap and create+ an almost uniform and symmetrical mass distribution. The writing speed of the nozzle was 50 mm min^{-1}. to ensure a thin deposit and the total deposition time was 2:40 min. Precise mass determination of particles impacted on a QCM assumes sufficient adherence of the particles. Chen *et al* (2016) tested this assumption by impacting various particles on QCMs and found excellent agreement with classic aerosol measurement instruments [24]. Our system operates at a lower pressure and the nanoparticles are impacted on the electrode at supersonic speeds, which must result in even better contact with the electrode surface and each other with respect to the milder impactor of Chen *et al.* Therefore, it is safe to assume that here too, the nanoparticles will resonate with the crystal, satisfying the second condition.

The QCM setup consists of an OpenQCM 14 mm QCM quartz holder inside the deposition chamber connected to an Arduino Micro outside the chamber with modified OpenQCM software that samples every 200 ms with a 5 Hz resolution. 10 MHz quartz crystals were used with 6 mm diameter Au electrodes and a C constant of 4.42×10^{-9} g Hz^{-1} cm^{-1}. For all measurements, a stable baseline was established in the first 20 s before the nozzle moved to the QCM center. Printing starts after a 60 s waiting time and lasts for 2:40 min. Afterward, the nozzle moves back to the middle of the QCM, where it waits for 60 s before it moves away. The deposition path is shown in the supplementary information figure 1. The mass difference was calculated using the difference between the frequencies before and after the nozzle was above the QCM to eliminate the effect of the supersonic gas jet on the resonance frequency.

2.3. Imaging and profile measurements

Direct volume measurement on deposits on a QCM is not possible due to the low height of the deposits. Therefore, it is necessary to deposit thicker samples with the same settings immediately after a QCM measurement. On a separate sample, lines of 3 mm in length were printed at speeds of 1.0 or 0.5 mm min^{-1} on glass with an Al coating. The cross-sectional area of the line was measured using a physical profilometer (Dektak 150). Each line was measured twice and averaged to get the cross-sectional area. This area was multiplied by the distance the nozzle traveled in one minute to get

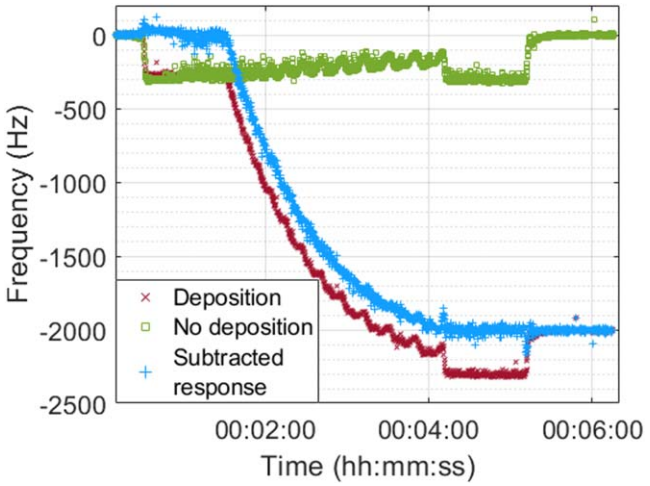

Figure 3. Frequency shift during deposition on the same QCM with (red) and without (green) nanoparticles in the gas. Subtracting the gas effect from the actual deposition results in the blue curve. The blue curve shows a profile with decaying mass deposition rate due to the reduced sensitivity of the QCM when printing closer to the edge. This sample was made with 5 mA and 1 mm nozzle distance.

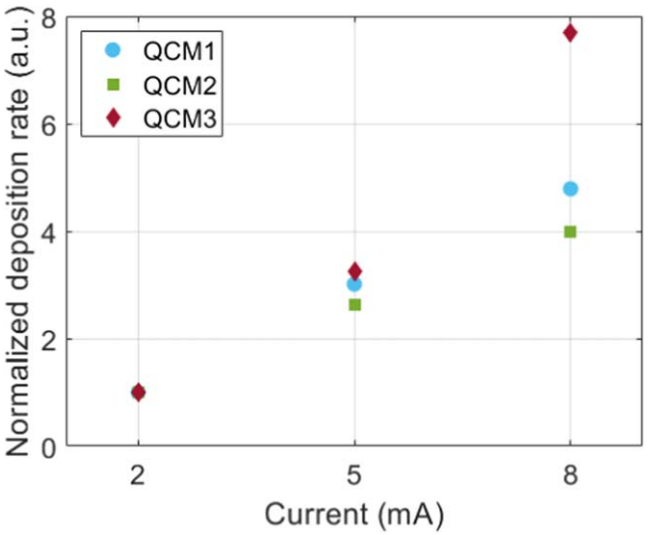

Figure 4. Normalized deposition rate plotted versus generator current for three QCMs. Per QCM, all data was collected in the same synthesis session to minimize fluctuations between depositions. Normalization per QCM was done with respect to the 2 mA sample for better comparison.

the volume of a one-minute deposit. The samples were imaged with a Hitachi Regulus 8230 SEM with a 5 kV acceleration voltage and a work distance of 5.0 mm and a Keyence VK-X250 optical microscope.

3. Results and discussion

3.1. QCM results

Figure 3 shows the typical response curve obtained during deposition, as well as the curve with the generator switched off. The effect of the gas jet on the QCM can be clearly seen when 'depositing' without aerosol, but in the end results in no mass change. The origin of this gas jet damping is unclear, and nearly no literature has been written on this. Kashan *et al* (2017) report on insignificant frequency changes (20 Hz per 50 kPa) in response to pressure change in vacuum [43]. It is possible that the force of the jet causes mechanical stress or even warping of the crystal, influencing its response. The sinusoidal waves in the QCM data are a direct result of the circular pattern, as shown in figure 1 in the supporting information. The time between two peaks increases due to the increase in diameter of each consecutive circle; the last one having a diameter of 17.6 mm and a deposition time of 21.1 s (more are shown in supporting information table 1). The peaks of each wave coincide with the left side of the QCM, since each circle starts and ends there. Between peaks, a small bump or plateau appears that must logically be on the right side of the QCM. The explanation of the non-uniform response to the gas flow with respect to the circle arc can only be explained by the geometry of the holder, since it is nearly identical for each QCM. One half of the sensor and most of the left and right sides have the edge of the QCM holder around it, which will disturb the gas flow and results in varying forces and pressures on each area. The decaying frequency change must not be confused with a decay in deposition rate, but is solely the result of the reduced responsivity of the QCM when moving towards the edge of the electrode area. The amplitude has a Gaussian distribution around the center and decreases to near zero at the electrode edges [28, 29, 44]. For this reason, it is not possible to extract a deposition rate from two arbitrary points during deposition; the whole curve must be used. To calculate the total frequency change, the average of the first and last 5 s of the entire curve are used to exclude any interference by the gas jet.

Mass generation in spark ablation is directly proportional to spark frequency, which scales linearly with increasing spark current following equation (2) [13, 40, 45]

$$f_s = I/2CV, \tag{2}$$

where I is the average current, V the electrode gap voltage at gas breakdown and C the capacitance of the generator's capacitors completely discharged into each spark. Results of varying generator current are plotted in figure 4 for three QCMs. Our prototype equipment gives considerable variations between experimental sessions, so for the sake of comparison, generation rates are normalized to the 2 mA data point. The increase in deposition rate is nearly linear, as expected from equation (2). For 5 mA, a mean deposition rate of 0.54 ± 0.22 μg was obtained. It must be noted that not all ablated mass reaches the sample. The nozzle has a throughput of $0.32\,\mathrm{l\,min^{-1}}$, which is 21% of the flow through the generator. Additional losses occur in the generation chamber due to turbulent gas flow and in the tubing due to diffusion to the walls. These losses were not quantified in this experiment, but considering that the deposition rate follows the expected linear scaling with increasing spark current, it appears these losses scale linearly as well or remain constant.

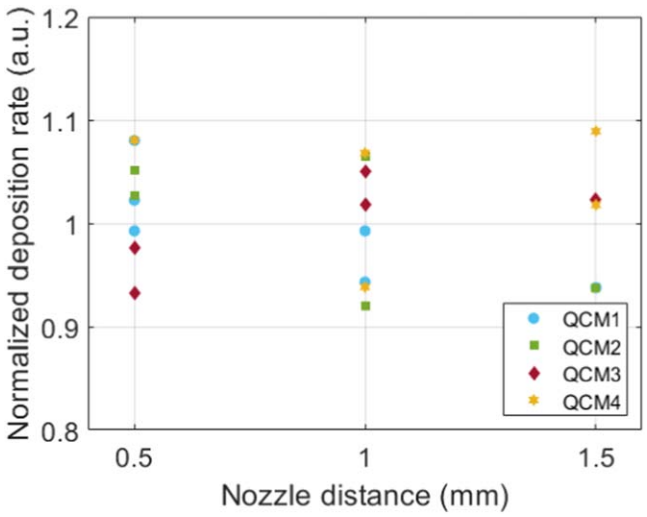

Figure 5. Deposition rate as a function of nozzle distance. Per QCM, all data was collected in the same synthesis session to minimize fluctuations between depositions. The data points are normalized to the mean per QCM for better comparison.

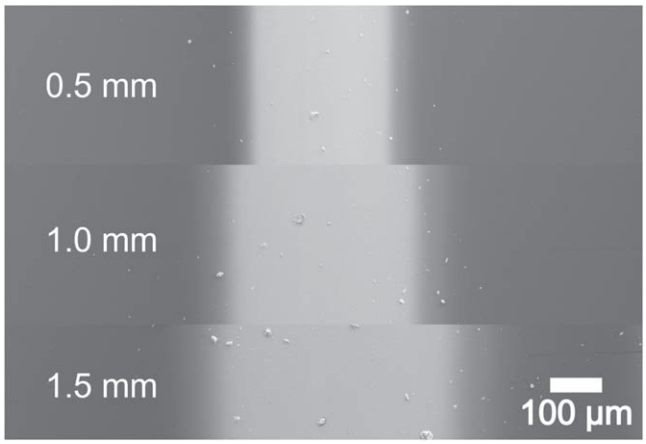

Figure 6. Compound SEM image (taken at 5 kV) of three lines printed after each other with nozzle distances of 0.5 mm, 1.0 mm, and 1.5 mm. The deposition rate of the nozzle is assumed constant as these lines are printed immediately after each other with identical settings. Provided the impaction efficiency remains the same for all distances, the mass of each line should be equal.

The nozzle-substrate distance was varied to investigate its effect. A larger distance gives the aerosol more time to decelerate and will lower the impaction energy. The particle trajectories can be considered ballistic for small distances, but diffusional motion should play a larger role as the distance is increased. Figure 5 shows the results for 4 QCMs normalized to the mean of their deposition rate. It can be seen that the depositions all fall within 10% of the mean rate and no clear trend can be identified. This indicates that the deposition rate is insensitive to the nozzle distance. This suggests that the impaction efficiency must be the same for the investigated distances, that is, 100% [41, 46]. The impaction jet has a conical shape, hence moving further away will increase the deposition area, as seen in figure 6.

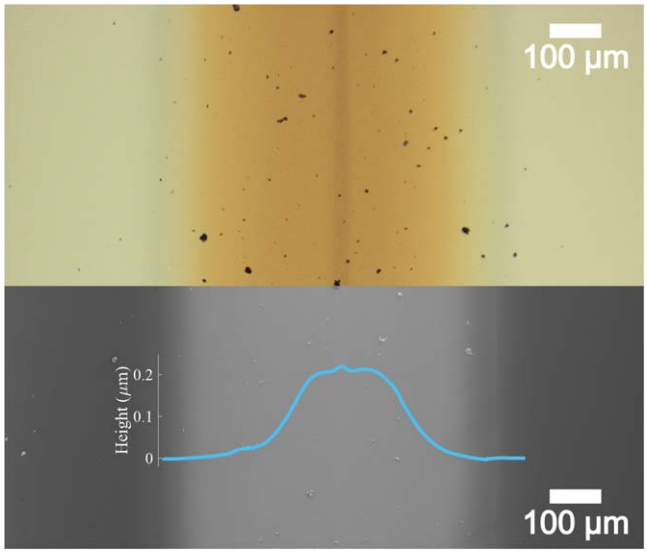

Figure 7. Compound image of an optical and scanning electron microscope image (taken at 5 kV) of a printed line on an Al surface. The profile in blue is an average of two Dektak profile measurements on two separate places with the peak at its approximate location overlaid on the image and with the same scale as the SEM image on its horizontal axis. Nozzle distance of 1 mm, 0.5 mm min^{-1}. writing speed, 5 mA generator current.

3.2. Porosity results

The first step in determining porosity is the determination of volume. Figure 7 shows the profilometric results for one line. The cross-section in figure 7 shows the line has a Gaussian shape at the edges and the center looks flatter. The deposit is not perfectly symmetrical due to imperfections in the nozzle and turbulence in the gas jet [41]. Asymmetry is not an issue for porosity determination but is something to consider when the surface profile is important. The deposits show some larger clusters, which accumulate over time and are clearly visible for longer deposition periods, e.g. for writing a line. Such clusters are rare at high nozzle speeds over wider areas (as is the case on the QCMs). The mean volume for a 5 mA, 1 mm sample is $4.46 \times 10^{-8} \pm 1.82 \times 10^{-8}\ \mu\text{m}^3$.

Porosity is defined as the fraction of the volume that is not occupied by the nanoparticles: $\Theta_p = V_{\text{film}}/V_{\text{total}}$. Alternatively, if those volumes are not readily available, the density ratio can also be used:

$$\Theta_p = 1 - \rho_{\text{film}}/\rho_{\text{Au}}, \tag{3}$$

where ρ_{film} is the density of the film and ρ_{Au} the density of bulk gold, 19.32 g cm^{-3}. Figure 8 shows a plot of the deposition rates and their corresponding volume measurement. The data shows a good fit through zero, from which we conclude that the porosity does not strongly depend on generation or deposition settings. Applying equation (3) using the density given by the slope of the fit in figure 8 gives a porosity of $\Theta_p = 0.18$. As the layer volume is proportional to the mass added, the layer porosity is constant. In agreement with the small value of Θ_p, SEM images such as in figure 9 show the film is dense and that individual nanoparticles have coalesced.

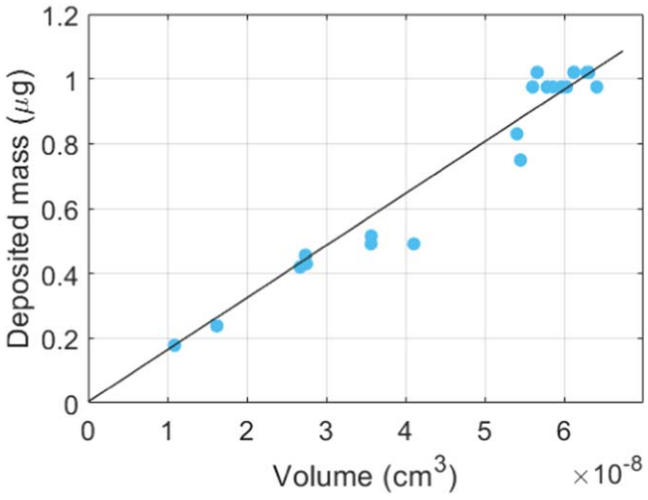

Figure 8. Relation between volume and mass of 1 min of deposition. A good linear fit through zero ($R^2 = 0.95$) shows the independence of the density to the deposition settings. The slope gives a density of 15.95 g cm^{-3}.

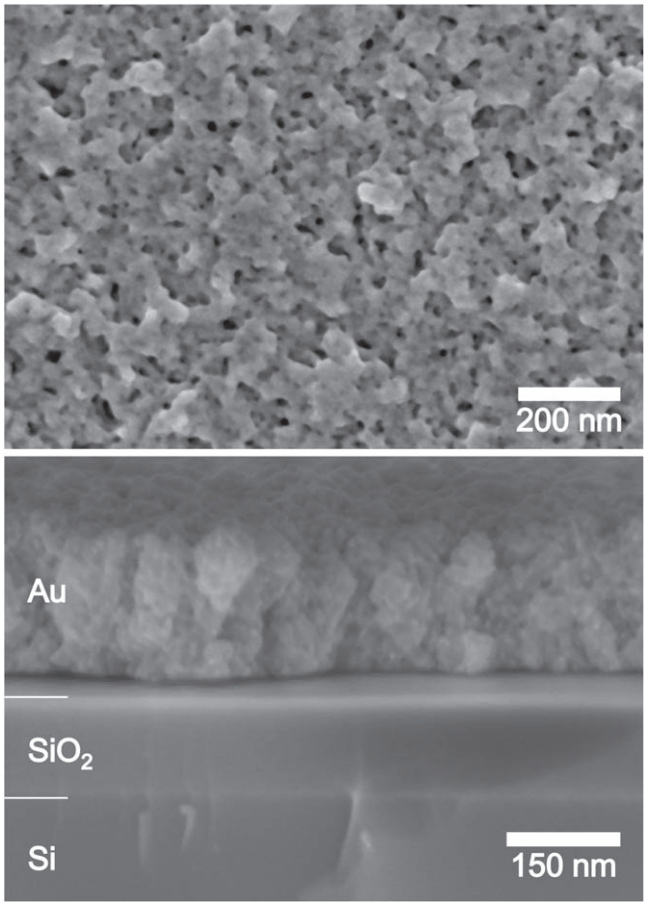

Figure 9. Tilted SEM images (taken at 5 kV) of a line printed at 1 mm min.$^{-1}$, 1 mm nozzle distance and 5 mA generator current. The surface (top) shows a high degree of nanoparticle coalescence and a porous structure. The bottom image shows a cross-section of a cleaved sample. The Si and SiO_2 layer are visible and labeled and the boundaries are marked. The nanoparticle film shows a 150 nm thick uniform film with dense nanoparticle structures.

Previous models by Lindquist *et al* [47] and Mädler *et al* [48] reported a porosity of 0.84 when they modeled ballistic deposition of equally sized spheres. Those models assume unagglomerated nanoparticles without inter-particle interactions. There are a few differences compared to those models that could probably explain the discrepancy with the results of this study. Firstly, Lindquist *et al* identify three regions with different porosities within their films [47]. Over time the porosity of region II, the middle region, starts to dominate. Region I (close to the substrate) and III (the surface) are finite in size, but region II keeps growing as the layer thickens. The reported porosity is the value of region II, but they note that at the start of deposition, when most of the film is in region I, the film approaches zero porosity. They define region I to end around 50 particle radii, here corresponding to 300–500 nm, higher than the peak in figure 7. Hence, if the model applies to our situation, the largest part of our sample should have a porosity smaller than 84%, and that porosity should increase with growing layer thickness. However, our experiment indicates that the layer density and therewith its porosity is constant. We believe that the lacking match between the simulations cited and our experiment originates from the fact that the process of impaction causes compaction of the film. Intuitively, a constant porosity induced by impaction pressure is not surprising, because portions with a higher porosity are more fragile and are compacted more strongly.

Lastly, if the impaction velocity is high enough, the kinetic energy can deform the particles themselves and induce sintering [13, 49]. A fundamental assumption in most deposition models is that such deformations do not occur, but the pristine surface of spark ablation generated Au nanoparticles make sintering upon impact likely. The absence of any surfactants or organic contaminants make the particle surfaces atoms mobile and reactive. SEM images seem to support this (figure 9), as they show a dense surface layer with nearly indistinguishable primary particles. The golden color of the deposits, as seen in figure 7, also indicates that the particles are (partially) fused together and act optically as bulk gold. Unsintered agglomerates of nanoparticles of 5–20 nm in diameter would appear black [14].

4. Conclusions

This method enables the direct measurement of the deposition rate in printed nanoporous thin films and, with the addition of volume data, porosity. It was found that the deposition rate increases linearly with generation current and is insensitive to nozzle distance at the tested distances. Hypersonically impaction printed Au nanoparticle films have a density of 15.95 g cm^{-3}, which translates to a constant porosity of 0.18. This is significantly lower than what previous simulations on impacted nanoparticle aerosols have found. We conclude that these simulations do not correctly describe the process of impaction printing, because a high degree of compaction and sintering takes place due to the impaction energy released. Our method has thus been applied to show that impaction printing is a method of producing layers of constant porosity.

Changes in density with height, creating an often called fractal or fractal-like structure, do not occur. The simulations predicting these do not consider reconstruction due to particle impact, and this may be correct for 'soft' deposition by diffusional transport but not for supersonic impaction printing. The measurement setup requires cheap and widely available components, so it is an accessible and simple method to determine porosity in nanoporous thin films. For process control, this method can already be applied with a simple QCM module in the printing chamber to monitor the mass deposition rate. Now that this method of determining the mass output of a spark generation aerosol printer is demonstrated, it can be validated for other metals, oxides, and ceramic nanoparticles.

Acknowledgments

We would like to acknowledge the funding by NWO Grant 729.001.023. We also thank the Else Kooi Laboratory and its staff for their technical support in the lab and VSPARTICLE B.V. for the use of their equipment in our laboratory.

Data availability statement

The data that support the findings of this study are available upon reasonable request from the authors.

Conflicts of interest

There are no conflicts to declare.

ORCID iDs

Hendrik Joost van Ginkel https://orcid.org/0000-0003-2143-9293
Sten Vollebregt https://orcid.org/0000-0001-6012-6180
Andreas Schmidt-Ott https://orcid.org/0000-0002-6312-2684

References

[1] Olveira S, Forster S P and Seeger S 2014 Nanocatalysis: academic discipline and industrial realities *J. Nanotechnol.* **2014** 1
[2] Guo S, Zhang S and Sun S 2013 Tuning nanoparticle catalysis for the oxygen reduction reaction *Angew. Chem. Int. Ed.* **52** 8526
[3] Mitsudome T and Kaneda K 2013 Gold nanoparticle catalysts for selective hydrogenations *Green Chem.* **15** 2636
[4] Aruna I, Kruis F E, Kundu S, Muhler M, Theissmann R and Spasova M 2009 Co ppb sensors based on monodispersed snox:pd mixed nanoparticle layers: Insight into dual conductance response *J. Appl. Phys.* **105** 064312
[5] Erol A, Okur S, Comba B, Mermer and Arıkan M 2010 Humidity sensing properties of ZnO nanoparticles synthesized by sol-gel process *Sensors Actuators* B **145** 174
[6] Mädler L, Roessler A, Pratsinis S, Sahm T, Gurlo A, Barsan N and Weimar U 2006a Direct formation of highly porous gas-sensing films by *in situ* thermophoretic deposition of flame-made pt/SnO2 nanoparticles *Sensors Actuators* B **114** 283
[7] Li Y, Moon K-S J and Wong C 2010 Nano-conductive adhesives for nano-electronics interconnection *Nano-Bio-Electronic, Photonic and MEMS Packaging* ed C Wong, K-S Moon and Y G Li (US, Boston, MA: Springer) pp 19–45
[8] Zhang B, Damian A, Zijl J, van Zeijl H, Zhang Y, Fan J and Zhang G 2021 In-air sintering of copper nanoparticle paste with pressure-assistance for die attachment in high power electronics *J. Mater. Sci., Mater. Electron.* **32** 4544
[9] Liu J, Chen H, Ji H and Li M 2016 Highly conductive cu-cu joint formation by low-temperature sintering of formic acid-treated cu nanoparticles *ACS Appl. Mater. Interfaces* **8** 33289
[10] He Y, Li X and Swihart M T 2005 Laser-driven aerosol synthesis of nickel nanoparticles *Chem. Mater.* **17** 1017
[11] Swihart M T 2003 Vapor-phase synthesis of nanoparticles *Curr. Opin. Colloid Interface Sci.* **8** 127
[12] Jia C-J and Schüth F 2011 Colloidal metal nanoparticles as a component of designed catalyst *Phys. Chem. Chem. Phys.* **13** 2457
[13] Pfeiffer T, Feng J and Schmidt-Ott A 2014 New developments in spark production of nanoparticles *Adv. Powder Technol.* **25** 56
[14] Schmidt-Ott A 2020 *Spark Ablation: Building Blocks for Nanotechnology* ed A Schmidt-Ott I edn (New York: Jenny Stanford Publishing) (https://doi.org/10.1201/9780367817091)
[15] Becker R, Weber K, Pfeiffer T V, van Kranendonk J and Schouten K J 2020 A scalable high-throughput deposition and screening setup relevant to industrial electrocatalysis *Catalysts* **10** 1165
[16] Valenti M, Dolat D, Biskos G, Schmidt-Ott A and Smith W A 2015 Enhancement of the photoelectrochemical performance of CuWO4 thin films for solar water splitting by plasmonic nanoparticle functionalization *J. Phys. Chem.* C **119** 2096
[17] Isaac N A, Valenti M, Schmidt-Ott A and Biskos G 2016 Characterization of tungsten oxide thin films produced by spark ablation for NO2 gas sensing *ACS Appl. Mater. Interfaces* **8** 3933
[18] Avdogmus H, van Ginkel H J, Galiti A-D, Hu M, Frimat J-P, Maagdenberg A V D, Zhang G, Mastrangeli M and Sarro P M 2021 Dual-gate fet-based charge sensor enhanced by *in situ* electrode decoration in a MEMS organs-on-chip platform *2021 21st Int. Conf. on Solid-State Sensors, Actuators and Microsystems (Transducers), IEEE*
[19] Aghajani S, Accardo A and Tichem M 2020 Aerosol direct writing and thermal tuning of copper nanoparticle patterns as surface-enhanced raman scattering sensors *ACS Appl. Nano Mater.* **3** 5665
[20] Kohut A, Horváth V, Pápa Z, Vajda B, Kopniczky J, Galbács G and Geretovszky Z 2021 One-step fabrication of fiber optic SERS sensors via spark ablation *Nanotechnology* **32** 395501
[21] Yu W, Batchelor-McAuley C, Wang Y-C, Shao S, Fairclough S M, Haigh S J, Young N P and Compton R G 2019 Characterising porosity in platinum nanoparticles *Nanoscale* **11** 17791
[22] Sinha P, Datar A, Jeong C, Deng X, Chung Y G and Lin L-C 2019 Surface area determination of porous materials using the Brunauer–Emmett–Teller (BET) method: limitations and improvements *J. Phys. Chem.* C **123** 20195

[23] Hering S V 1987 Calibration of the QCM impactor for stratospheric sampling *Aerosol Sci. Technol.* **7** 257
[24] Chen M, Romay F J, Li L, Naqwi A and Marple V A 2016a A novel quartz crystal cascade impactor for real-time aerosol mass distribution measurement *Aerosol Sci. Technol.* **50** 971
[25] Marple V, Rubow K, Ananth G and Fissan H 1986 Micro-orifice uniform deposit impactor *J. Aerosol Sci.* **17** 489
[26] Kolasinski R D, Polk J E, Goebel D and Johnson L K 2008 Carbon sputtering yield measurements at grazing incidence *Appl. Surf. Sci.* **254** 2506
[27] Leskelä M and Ritala M 2002 Atomic layer deposition (ALD): from precursors to thin film structures *Thin Solid Films* **409** 138
[28] Sauerbrey G 1959 Verwendung von schwingquarzen zur wëgung dünner schichten und zur mikrowëgung *Z. für Phys.* **155** 206
[29] van der Steen C, Boersma F and van Ballegooyen E C 1977 The influence of mass loading outside the electrode area on the resonant frequencies of a quartz-crystal microbalance *J. Appl. Phys.* **48** 3201
[30] Benes E 1984 Improved quartz crystal microbalance technique *J. Appl. Phys.* **56** 608
[31] Lu C-S and Lewis O 1972 Investigation of film thickness determination by oscillating quartz resonators with large mass load *J. Appl. Phys.* **43** 4385
[32] Fischerauer G and Dickert F L 2016 A simple model for the effect of nonuniform mass loading on the response of gravimetric chemical sensors *Sensors Actuators* B **229** 618
[33] Chen Q, Xu S, Liu Q, Masliyah J and Xu Z 2016b QCM-d study of nanoparticle interactions *Adv. Colloid Interface Sci.* **233** 94
[34] Jiang H and Tang L 2021 Uniformization of QCM's mass sensitivity distribution by optimizing its metal electrode configurations *IEEE Sensors J.* **21** 9008
[35] Sun P, Jiang Y, Xie G, Du X and Hu J 2009 A room temperature supramolecular-based quartz crystal microbalance (QCM) methane gas sensor *Sensors Actuators* B **141** 104
[36] Ding B, Kim J, Miyazaki Y and Shiratori S 2004 Electrospun nanofibrous membranes coated quartz crystal microbalance as gas sensor for NH3 detection *Sensors Actuators* B **101** 373
[37] Morelli L, Ricciardella F, Koole M, Persijn S and Vollebregt S 2020 Functionalisation of multi-layer graphene-based gas sensor by au nanoparticles *IV Int. Conf. nanoFIS 2020—Functional Integrated Nanosystems MDPI*
[38] Bonroy K, Friedt J-M, Frederix F, Laureyn W, Langerock S, Campitelli A, Sára M, Borghs G, Goddeeris B and Declerck P 2004 Realization and characterization of porous gold for increased protein coverage on acoustic sensors *Anal. Chem.* **76** 4299
[39] Mannelli I, Minunni M, Tombelli S and Mascini M 2003 Quartz crystal microbalance (QCM) affinity biosensor for genetically modified organisms (GMOs) detection *Biosens. Bioelectron.* **18** 129
[40] Feng J, Huang L, Ludvigsson L, Messing M E, Maisser A, Biskos G and Schmidt-Ott A 2015 General approach to the evolution of singlet nanoparticles from a rapidly quenched point source *J. Phys. Chem.* C **120** 621
[41] Rennecke S and Weber A 2013 A novel model for the determination of nanoparticle impact velocity in low pressure impactors *J. Aerosol Sci.* **55** 89
[42] Holman Z C and Kortshagen U R 2010 A flexible method for depositing dense nanocrystal thin films: impaction of germanium nanocrystals *Nanotechnology* **21** 335302
[43] Kashan M A M, Kalavally V, Mazumdar P, Lee H W and Ramakrishnan N 2017 QCM coupled resonating systems under vacuum: Sensitivity and characteristics *IEEE Sensors J.* **17** 5044
[44] Huang X, Bai Q, Hu J and Hou D 2017 A practical model of quartz crystal microbalance in actual applications *Sensors* **17** 1785
[45] Tabrizi N S, Ullmann M, Vons V A, Lafont U and Schmidt-Ott A 2008 Generation of nanoparticles by spark discharge *J. Nanopart. Res.* **11** 315
[46] Li C, Singh N, Andrews A, Olson B A, Schwartzentruber T E and Hogan C J 2019 Mass, momentum, and energy transfer in supersonic aerosol deposition processes *Int. J. Heat Mass Transfer* **129** 1161
[47] Lindquist G J, Pui D Y and Hogan C J 2014 Porous particulate film deposition in the transition regime *J. Aerosol Sci.* **74** 42
[48] Mädler L, Lall A A and Friedlander S K 2006b One-step aerosol synthesis of nanoparticle agglomerate films: simulation of film porosity and thickness *Nanotechnology* **17** 4783
[49] Peineke C 2008 Production and deposition of well defined aerosol nanoparticles for studies of basic properties *PhD Thesis* Delft University of Technology